Journal of Power Sources 195 (2010) 1401–1407

Contents lists available at ScienceDirect

Journal of Power Sources

journal homepage: www.elsevier.com/locate/jpowsour

Ex situ evaluation of nanometer range gold coating on stainless steel substrate for automotive polymer electrolyte membrane fuel cell bipolar plate

A. Kumar*, M. Ricketts, S. Hirano

Ford Motor Company, 2101 Village Road, Dearborn, MI 48121, USA

ARTICLE INFO

Article history:
Received 30 July 2009
Received in revised form 8 September 2009
Accepted 9 September 2009
Available online 16 September 2009

Keywords:
Fuel cell
Metal bipolar plate
Corrosion
Electrical conductivity

ABSTRACT

The bipolar plate in polymer electrolyte membrane (PEM) fuel cell helps to feed reactant gases to the membrane electrode assembly (MEA) and collect current from the MEA. To facilitate these functions, the bipolar plate material should exhibit excellent electrical conductivity and corrosion resistance under fuel cell operating conditions, and simultaneously be of low-cost to meet commercialization enabling targets for automotive fuel cells. In the present work, we focus on the benchmarking of 10 nm gold coated SS316L (a.k.a. Au Nanoclad®) bipolar plate material through ex situ tests, which is provided by Daido Steel (Japan). The use of nanometer range Au coatings help to retain the noble properties of gold while significantly reducing the cost of the bipolar plate. The area specific resistance of the flat sample is 0.9 mΩ cm^2 while that for the formed bipolar plate is 6.3 mΩ cm^2 at compaction force of 60 N cm^{-2}. The corrosion current density was less than 1 μA cm^{-2} at 0.8 V/NHE with air sparge simulating cathodic conditions. Additionally, gold coated SS316L showed anodic passivation of SS316L, thereby exhibiting robustness towards coating defects including surface scratches that may originate during the manufacturing of the bipolar plate. These series of ex situ tests indicate that 10 nm gold coated SS316L has good potential to be considered for commercial bipolar plates in automotive fuel cell stack.

1. Introduction

The need for thin and low-cost bipolar plates in automotive fuel cell stack has necessitated the use of metals/alloys as bipolar plate materials. Additionally, these materials need to be electrically conductive and corrosion resistant under fuel cell operating conditions to enable the bipolar plate to perform its functions—feeding reactant gases to membrane electrode assembly (MEA) and collecting current from MEA. In lieu of this, several researchers have proposed the use of Fe, Al, Cu, Ni, Ti-based alloys for bipolar plate substrate materials, with emphasis on Fe-based alloys like stainless steel [1–3]. Stainless steel is a low-cost, high strength, and readily available material. Stainless steel bipolar plates are easy to fabricate as thin sheets (~100 μm) can be shaped by mechanical deforming process (like stamping, corrugated rolling, etc.). However, bare stainless steel alloys are not suitable under PEM fuel cell operating conditions. Bare stainless steel alloy constituents slowly leach out of the bipolar plate that can poison other fuel cell stack components (notably membrane electrode assembly) [4]. Furthermore, bare stainless steel alloys form insulating passive layers under fuel cell operating conditions resulting in higher surface electrical resistance. This is clearly shown in the thermodynamic Eh–pH diagram for Fe (major alloying element in stainless steel) [5]. As is shown in Fig. 1a, Fe is stable in elemental form below −0.7 V/NHE in pH range of 3–5 (typical fuel cell pH range). In the fuel cell operating potential regime, Fe is stable either in the form of Fe^{2+} or Fe^{3+} oxidation states. These oxides of Fe (and similarly other stainless steel constituents like Cr, Ni) lead to high surface electrical resistance, and necessitate the need for coating material.

Several coating materials and processes have been proposed to improve the corrosion resistance and electrical conductivity of the base substrates [1]. One such material is gold (Au) which can be utilized as a coating for bipolar plates due to its high electrical conductivity and excellent corrosion resistance. The high corrosion resistance of Au is due to immunity in wide range of pH values. As shown in Fig. 1b, the zone of immunity extends to 1.2 V redox potential at lower pH, and 0.4 V redox potential under highly basic conditions. Gold as a coating material on stainless steel has been researched extensively, and several researchers have proposed the use of few micron of Au coating on bare bipolar plate substrate with great success [6]. However, stringent cost constraints for automotive fuel cell stack prohibit the use of Au in micron thickness range. On the other hand noble properties and high electrical conductivity of Au are most desirable for bipolar plate application in fuel cell.

Based on this concept, and keeping the cost constraints in mind, Daido Steel (Japan) developed gold coated stainless steel material

* Corresponding author at: Research and Advanced Engineering, Ford Motor Company, 2101 Village Road, Room 1213, Dearborn, MI 48121, USA.
Tel.: +1 313 206 3842; fax: +1 313 594 2963.
E-mail address: akumar56@ford.com (A. Kumar).

0378-7753/$ – see front matter © 2009 Elsevier B.V. All rights reserved.
doi:10.1016/j.jpowsour.2009.09.022

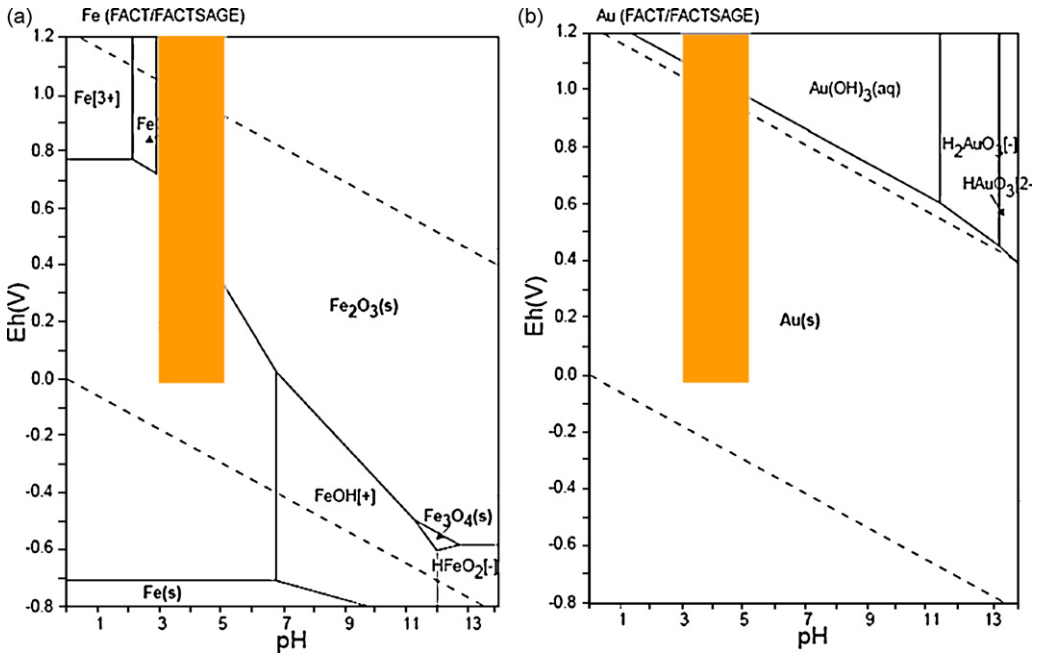

Fig. 1. Eh–pH diagrams for iron (a, left) and gold (b, right) (the fuel cell operating potential range and pH range are shown by the shaded areas in the graphs).

(a.k.a. Au Nanoclad®). This material has extremely thin Au layer (typically 10–40 nm) on the base substrate (SS316L) which significantly reduces the cost of the bipolar plate while retaining the desired characteristics of Au. Additional advantages accrue due to the pre-coating (coating before plate stamping) nature of the process that allows for better process control, and potentially high yield in manufacturing.

This paper presents the ex situ benchmarking test data for 10 nm thick Au on 100-μm gauge SS316L metal foil (hereafter refereed to as 10nm-Au/SS316L). It is important to mention that certain experiments were carried out with 20 nm thick Au on 100-μm gauge SS316L metal foil (hereafter refereed to as 20nm-Au/SS316L). These experiments were not part of the benchmarking metrics but were carried out for greater understanding of material behavior in fuel cells. It is expected that 10nm-Au/SS316L material exhibits similar behavior.

2. Verification test methods

The verification test methods and quality metrics that were used to benchmark 10nm-Au/SS316L material were developed to cover anticipated failure modes of bipolar plate material in the fuel cell. The test methods included all aspects for bipolar plate including materials, design, and manufacturing process.

2.1. Ex situ area specific resistance test

An increase in electrical resistance of the bipolar plate directly leads to performance loss in the fuel cell stack. This resistance can be divided into bulk resistance and contact resistance—both of which result in voltage drop across the bipolar plates. The bulk resistance is the resistance of the bipolar plate material, and the contact resistance is the resistance of the bipolar plate—gas diffusion layer interface. A method, similar to that described by Wang et al. [2] was used to measure the electrical resistance. Toray Carbon Paper (TGPH-060, non-teflonized) was used as gas diffusion layer in these experiments. The compression pressure of 60 N cm^{-2} is applied over 20 cm^2 circular electrode area to simulate stack conditions. The voltage drop can be measured by passing a measured current (20 A, corresponding to 1 A cm^{-2} over 20 cm^2 circular electrode area) through the sample cross-section and recording the potential drop across the sample. The area specific resistance (R_S) can then be calculated using Eq. (1):

$$R_S = \frac{VA_S}{I} \quad (1)$$

where V is the voltage drop, I is the current applied, and A_S is the surface area of the electrode.

Fig. 2 shows the picture and schematic sketch of the Through Plane Voltage (TPV) drop equipment. The equipment was devel-

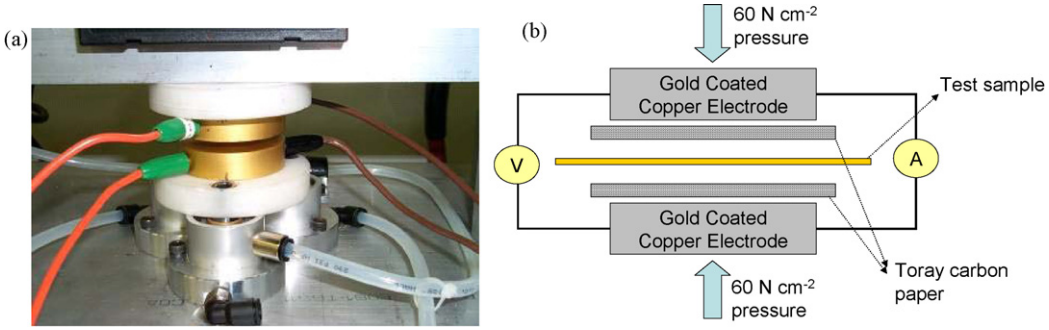

Fig. 2. Picture of Through Plane Voltage (TPV) drop equipment (a, left) and schematic diagram (b, right).

Table 1
Test conditions for cyclic voltammetry/potentiostatic experiments.

Test	Parameter	Condition
Cyclic voltammetry (CV)	Electrolyte	0.5 mM H_2SO_4 (pH 3)
	Temperature	80 °C
	Pretreatment	3 min cleaning at −0.44 V
	Scan rate	2 mV s^{-1}
	Start potential	−0.44 V/NHE
	Peak potential	+1.60 V/NHE
	End potential	−0.40 V/NHE
	Gas purging	Air|H_2
	Stirring	No
Potentiostatic	Electrolyte	0.5 mM H_2SO_4 (pH 3)
	Temperature	80 °C
	Pretreatment	No
	Potentials	+1.2, +1.4, +1.6 V/NHE (6 h); +0.8 V/NHE (24 h)|+0.1, +0.5 V/NHE (6 h)
	Gas purging	Air|H_2
	Stirring	No

oped to improve the consistency of the contact pressure by using a three-point circular anvil, with all three points connected to the same pressure supply. This eliminated the possibility of misalignment between the anvils and therefore provided a much more consistent pressure across the entire plate. In addition, the mating anvils were machined to a flatness of 5 μm.

2.2. Ex situ corrosion tests

Corrosion is an important quality metric for benchmarking bipolar plate materials. Corrosion experiments were performed using PAR electrochemical three-electrode cell, in which a graphite rod acted as the counter electrode, a saturated calomel electrode acted as the reference electrode, and test sample as the working electrode. The test conditions for the corrosion experiment are tabulated in Table 1 and were chosen to simulate real world fuel cell operating conditions. The electrolyte is 0.5 mM H_2SO_4 (pH 3) at 80 °C sparged with hydrogen and air to simulate anode and cathode conditions, respectively. Sample pretreatment step included a 3 min cleaning by holding the sample at −0.44 V/NHE for 3 min. Cyclic voltammograms (CV) was obtained in potential window of −0.44 to 1.6 V/NHE at scan rate of 2 mV s^{-1}. Potentiostatic experiments were performed at 0.1 and 0.5 V/NHE under anodic conditions and at 1.2, 1.4, and 1.6 V/NHE under cathodic conditions. The duration of these experiments were 6 h each, and were performed to demonstrate robustness of the plate material under certain fuel cell operating conditions (like fuel starvation, start-up/shut-down, etc.). An additional long term potentiostatic test was run at 0.8 V/NHE for 24 h under cathodic conditions to demonstrate durability of the plate material.

2.3. Ex situ mechanical tests

Metal bipolar plates are currently manufactured using a stamping process. The mechanical properties of sheet metal, along with manufacturing process determine the design space for the material. Standard ASTM tests (E8M, E646) were performed to determine the ultimate tensile strength (UTS), total elongation (% el), and strain hardening exponent (*n*-value) of 10nm-Au/SS316L material in rolling direction and parallel to rolling direction.

3. Results and discussion

3.1. Area specific resistance

The area specific resistance of as-received 10nm-Au/SS316L flat sheet is 0.9 mΩ cm^2. The Toray Carbon Paper reference values have been subtracted from the measurements. We also fabricated metal bipolar plate with 10nm-Au/SS316L material. Area specific resistance measurements were performed at 12 different locations on the plate. The average area specific resistance for 10nm-Au/SS316L bipolar plate is 6.3 mΩ cm^2.

3.2. Corrosion

Cyclic voltammetry and potentiostatic studies were performed on as-received 10nm-Au/SS316L flat sheet under simulated anodic and cathodic conditions. Robustness testing which included performing cyclic voltammetry on 10nm-Au/SS316L with different levels of coating defects was also performed. The results from these tests are detailed in the following sections.

3.2.1. Cyclic voltammetry—hydrogen sparge (anodic)

The cyclic voltammogram of 10nm-Au/SS316L with hydrogen sparge (simulating fuel cell anodic conditions) is shown in Fig. 3. A region of hydrogen evolution as suggested by Eh–pH diagram is observed at lower potentials. At intermediate potentials (0.1 V/NHE to around 1.1 V/NHE), Au is immune and consequently no faradic peaks are expected—only double layer charging is expected in this region. However, as is shown in figure, faradic behavior is observed in this region. Cyclic voltammetry was also performed on bare SS316L (substrate) under the same conditions. It was seen that bare SS316L showed a typical active–passive behavior—active peak at around −0.14 V/NHE, passive region at intermediate potentials, followed by trans-passive peak at around 1.1 V/NHE. It is important to

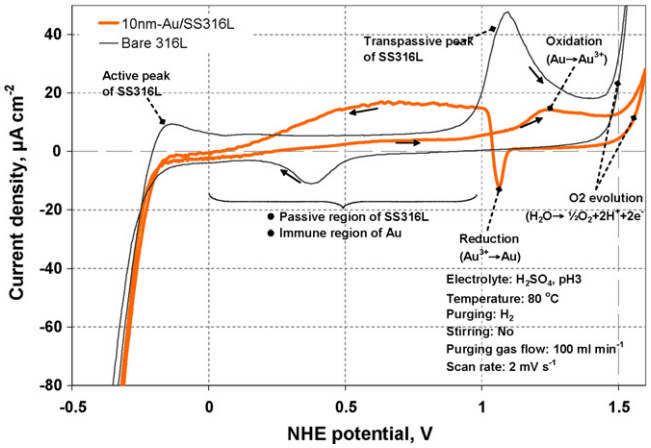

Fig. 3. Cyclic voltammogram for 10nm-Au/SS316L and bare SS316L in hydrogen sparge.

note that 10nm-Au/SS316L does not exhibit any active peak similar to the one exhibited by bare SS316L.

Further at high potentials in case of 10nm-Au/SS316L (1.1 V/NHE to around 1.4 V/NHE), surface oxidation of Au occurs. Surface oxidation (or reduction) processes are limited by the amount of material that can be deposited (or reduced in case of reduction)—leading to faradic peaks. It is interesting to note that first sweep has two oxidation peaks; however, the former peak disappears in subsequent scans. At higher potentials (around 1.6 V/NHE), oxygen evolution starts to occur—resulting in high current density.

On the reverse scan a reduction peak of Au is observed at around 1.15 V/NHE. Interestingly, immediately after this reduction peak, reactivated faradic oxidation peaks were observed. This peculiar behavior is again similar to what is observed with pure Au foil. So it was concluded that the appearance of unexpected faradic peaks in the double layer region is due to inherent property of Au, and not the 10nm-Au/SS316L. The objective for this further discussion is to understand the peculiar behavior of 10nm-Au/SS316L (similar with Au) under fuel cell anodic conditions. Experiments were performed with 20nm-Au/SS316L to understand any implication of this behavior on the fuel cell stack under real-world operating conditions. It is expected that 10nm-Au/SS316L exhibits similar behavior to 20nm-Au/SS316L material.

3.2.1.1. Oxidation and reduction of Au. Based on thermodynamics, oxidation of Au ($Au \rightarrow Au^{3+}$) occurs at standard reversible potential of 1.457 V/NHE if the product is hydrated oxide, or at 1.511 V/NHE if the product is anhydrous oxide [7]. As seen in Fig. 3, oxidation of Au starts at 1.15 V/NHE. This is not unusual and may be explained based on the fact that surface atoms are more active than their bulk equivalent, due to electrostatic adsorption of H_2O molecule on the surface. Consequently, the oxidation proceeds at lower potential than the thermodynamic value.

Furthermore, two main peaks are observed in the first scan in the oxidation region of Au at 1.297 and 1.381 V/NHE. The first peak is associated with formation of $Au(OH)_3$ followed by formation of oxide layer in the second peak. The first peak increases while the second peak decreases in subsequent scans. These compensatory changes are due to the effect of trace amounts of chloride and sulfate in the electrolyte [8]. On the reverse scan, the Au oxide layer reduction starts at around 1.1–1.2 V/NHE as shown in figure. The current peaks overlap up to the peak current, followed by appearance of unexpected anodic oxidation peaks (during reverse scans).

3.2.1.2. Double layer charge region. Hydrogen oxidation ($H_2 \rightarrow 2H^+ + 2e^-$) is expected thermodynamically at 0 V/NHE on some noble metals like Pt. This is because Pt helps in breaking the H–H bond by dissociative chemisorption. However, in case of Au, H_2 is not dissociatively adsorbed, and consequently, no faradic oxidation peaks should appear.

As seen in the Eh–pH diagram gold does not exhibit faradic behavior in between 0 and 1.0 V/NHE. However as seen in Fig. 3, oxidation peaks appear both during the forward and reverse scans. Oxidation peak during the forward scan becomes prominent around 0.2 V/NHE, and decreases when the gold oxidation peak starts at around 1.1 V/NHE. The oxidation peak during the reverse scans appears immediately after the gold reduction peak.

The phenomena of faradic peaks can be explained by first looking carefully at the double layer charge region in nitrogen. Fig. 4 shows the cyclic voltammogram of 20nm-Au/SS316L in nitrogen sparge (Run 1). As expected, no faradic peaks are observed. The oxidation peaks in hydrogen sparge can be explained based on the strong HSO_4^- anion chemisorption that occurs during this double layer region (a partially resolved peak is visible during the nitrogen sparge at around 0.5 V/NHE). During the hydrogen sparge (Fig. 4, Run 2), the chemisorbed HSO_4^- are discharged which mediates

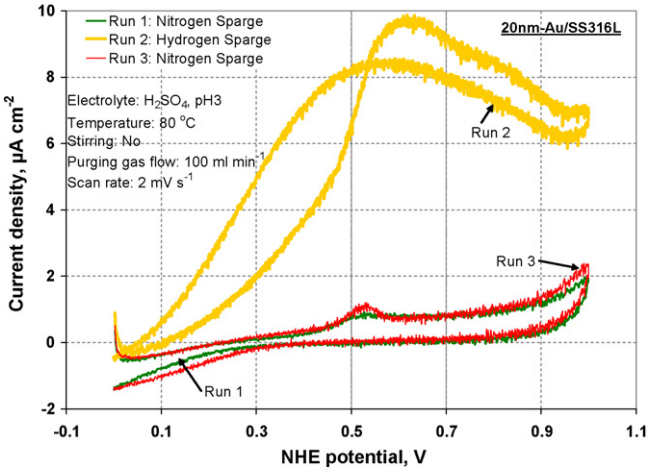

Fig. 4. Double layer charge region with nitrogen sparge (Run 1, green), hydrogen sparge (Run 2, gold), followed by nitrogen sparge (Run 3, red) for 20nm-Au/SS316L material. (For interpretation of the references to color in this figure legend, the reader is referred to the web version of the article.)

the breaking of H–H bond. This occurs by withdrawal of an electron from HSO_4^- ion. The electron from this chemisorbed HSO_4^- species mediates the breaking of H–H bond. Run 3 with nitrogen sparge shows no (or minimal) change in the double layer charge behavior. This demonstrates that hydrogen oxidation peaks do not change the double layer behavior (or surface morphology) of Au when cycled in between 0.0 and 1.0 V/NHE potential range.

At voltages around 1.0 V/NHE and higher, the appearance of gold hydroxide (or oxide) stops the hydrogen oxidation reaction. Once the reduction of oxide layer starts, and free Au surface sites are available, chemisorbed anions are again discharged leading to the start of the hydrogen oxidation reaction during the reverse scan.

One of the possible hypotheses for the appearance of the oxidation peaks in the double layer region was the formation of defective structure during the reduction of gold surface oxide layer. As reported in literature [9], the presence of such an active structure could facilitate and accelerate the anodic processes. Consequently, experiments were performed in different potential ranges. As is seen in Fig. 5, oxidation peaks in both reverse and forward scans are observed in all potential ranges. However, faradic currents for the peaks where potential range was less than gold oxidation were similar (forward scans for 0.0–0.5, 0.0–0.8, and 0.0–1.1 V/NHE).

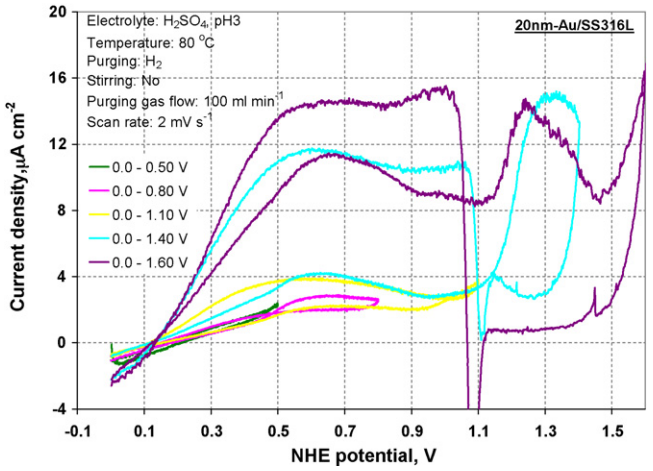

Fig. 5. Effect of potential scan range on the oxidation peaks in the double layer region of 20nm-Au/SS316L material: (a) 0.0–0.50 V/NHE; (b) 0.0–0.80 V/NHE; (c) 0.0–1.10 V/NHE; (d) 0.0–1.40 V/NHE; and (e) 0.0–1.60 V/NHE.

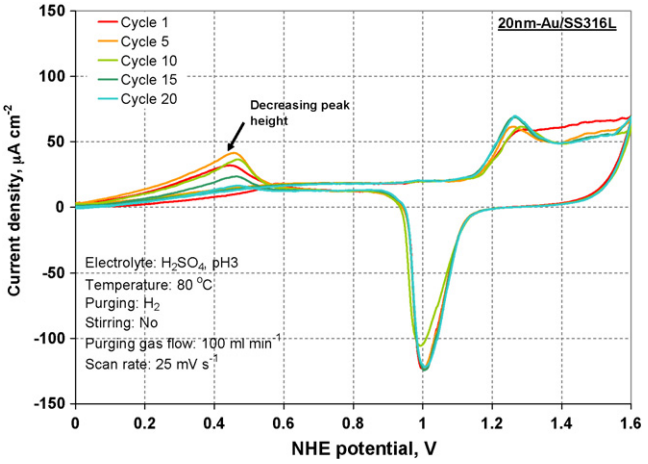

Fig. 6. Effect of cycling on the hydrogen oxidation peaks in the double layer region and gold oxidation/reduction peaks for 20nm-Au/SS316L material.

Potential ranges which involved oxidation/reduction of gold saw an increased faradic current in the double layer region of gold.

3.2.1.3. Implication on bipolar plates. The hydrogen oxidation reaction is believed to have no implication on the bipolar plates. This is clear from the several cycles of cyclic voltammogram that were performed on the 20nm-Au/SS316L. Between each cycle, 1 h constant potentiostatic run at 0.5 V/NHE was performed. Fig. 6 shows the effect of 20 cycles on the hydrogen oxidation peak in the double layer region and oxidation/reduction peaks for Au. Hydrogen oxidation peak currents in general decrease with number of scans, while no significant change in the oxidation/reduction peaks of Au is observed. The decrease in hydrogen oxidation peak current is due to increased presence of Au oxide compounds on the surface of Au. Furthermore, no additional peaks corresponding to SS316L base substrate, which proves that 20nm-Au/SS316L coating was not compromised because of hydrogen oxidation reactions.

3.2.2. Cyclic voltammetry—air sparge (cathodic)

The cyclic voltammogram of 10nm-Au/SS316L with air sparge (simulating fuel cell cathodic conditions) is shown in Fig. 7. A region of hydrogen evolution as suggested by Eh–pH diagram is observed at lower potentials. At intermediate potentials (0.45 V/NHE to around 1.1 V/NHE), Au is immune and consequently no faradic peaks are observed—only double layer charging is observed. Current density in this potential range is less than around 2 $\mu A\,cm^{-2}$.

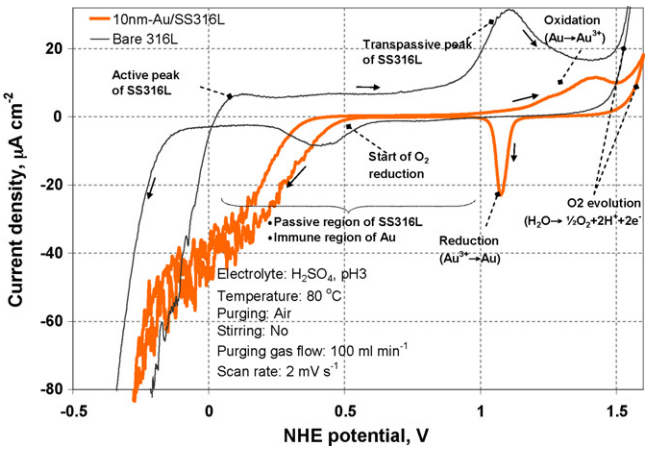

Fig. 7. Cyclic voltammogram for 10nm-Au/SS316L and bare SS316L in air sparge.

The current density at 0.8 V/NHE is 0.94 $\mu A\,cm^{-2}$. Further at high potentials (1.1 V/NHE to around 1.4 V/NHE) in case of 10nm-Au/SS316L surface oxidation of Au occurs. At higher potentials (around 1.6 V/NHE), oxygen evolution starts to occur—resulting in high current density.

On the reverse scan a reduction peak of Au ($Au^{3+} \rightarrow Au$) is observed at around 1.15 V/NHE. At around 0.45 V/NHE, the oxygen reduction reaction (ORR) peak is observed in the reverse scan. Thermodynamically, two reactions for O_2 reduction are possible under acidic conditions:

$2e^-$ reduction of O_2 on Au (1 1 1), (1 1 0) surface

$$O_2 + 2H^+ + 2e^- \rightarrow H_2O_2 \quad (a)$$

$4e^-$ reduction of O_2 on Au (1 0 0) surface

$$O_2 + 4H^+ + 4e^- \rightarrow 2H_2O \quad (b)$$

The effectiveness of H_2O_2 formation on 10nm-Au/SS316L bipolar plate is very minimal under fuel cell operating conditions. The equilibrium potential (0.45 V/NHE) for H_2O_2 formation is more probable on the anode side than cathode side. Furthermore, this ORR is mass transport limited process and has very minimal probability of happening on anode side (due to oxygen gas cross-over to anode). Consequently, ORR peaks have no implication on the performance of bipolar plate made with 10nm-Au/SS316L material.

3.2.3. Potentiostatic (constant potential)

The results for the potentiostatic experiments for 10nm-Au/SS316L material under hydrogen (at 0.1 and 0.5 V/NHE) and air (1.2, 1.4, and 1.6 V/NHE) sparge for 6 h are shown in Fig. 8. It is important to note that typical fuel cell potentials for anode side is around 0 V/NHE, while that for the cathode side is around 0.8 V/NHE. However, under certain conditions (like start-up/shut-down, freeze start-up, etc.) the electrode potential may rise to higher values. Consequently, testing at higher potentials is warranted in the potentiostatic experiments to demonstrate the robustness of the material. Results indicate very low and stable current densities (<10 $\mu A\,cm^{-2}$) for most cases except 1.6 V/NHE (air) case where slightly higher current density (~60 $\mu A\,cm^{-2}$) was observed. For 1.6 V/NHE (air) case, a cyclic voltammogram scan was also performed on sample after 6 h potentiostatic run. The current density at 0.8 V/NHE (air) obtained from this cyclic voltammogram was around 1 $\mu A\,cm^{-2}$, thereby demonstrating no significant change in the 10nm-Au/SS316L. Additionally, for all the potentiostatic runs, no corrosion was observed on sample exposed area.

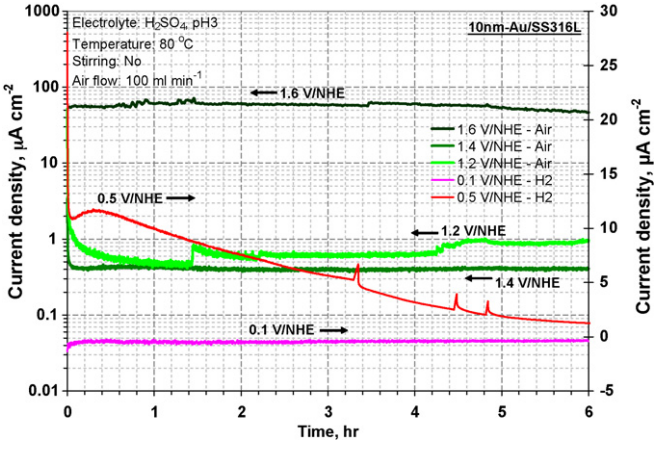

Fig. 8. Potentiostatic experiments of 10nm-Au/SS316L in H_2 (at 0.1 and 0.5 V/NHE) and air (at 1.2, 1.4, and 1.6 V/NHE) for 6 h.

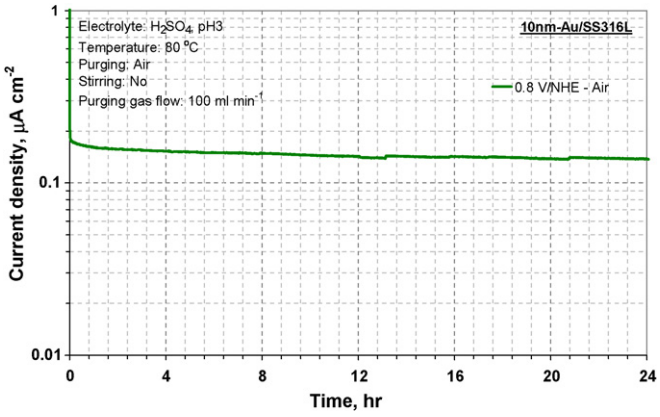

Fig. 9. Potentiostatic experiments of 10nm-Au/SS316L in air at 0.8 V/NHE for 24 h.

Area specific resistance measurements were also performed on the exposed samples; and no statistical change in value was observed in any of the 5 experiments.

An additional long term potentiostatic test was run at 0.8 V/NHE for 24 h under cathodic conditions to simulate durability behavior for the 10nm-Au/SS316L. As shown in Fig. 9, the current density was less than 0.2 μA cm^{-2} for the period of the experiment. No corrosion on sample was observed after the test.

3.2.4. Anodic passivation protection

Coating defects (scratches, indents, etc.) on the bipolar plate can originate during the coating process or afterwards during handling or stack assembly. Although, the intent is to implement quality control at each step in the manufacturing process, it is worthwhile to develop a technology that is robust to coating defect—at least to a certain extent. The Au Nanoclad material was developed by Daido Steel utilizing the anodic passivation protection phenomena [10]. This means that even if there are some scratches or uncoated area on the bipolar plate, the coated regions will provide some level of protection by promoting the passivation of stainless steel. This happens typically when the anodic polarization curve of SS316L and cathodic polarization curve of Au intersect in the SS316L passive area. Furthermore, this phenomenon also provides protection to the uncoated edges (especially in the manifold) of the plate.

Experiments as described in this section were performed with 20nm-Au/SS316L material to validate the anodic polarization protection concept. It is expected that 10nm-Au/SS316L exhibits similar behavior to 20nm-Au/SS316L material. To simulate scratches or uncoated area, five samples were tested with different coverage of Au (0%, 25%, 50%, 75%, 100% Au coverage). The 0% Au coverage indicated SS316L with no coating, while 100% Au coverage indicates normal 20nm-Au/SS316L material. Cyclic voltammetry studies were performed on these five samples and the results are described below.

Fig. 10 shows the Tafel plots for five samples with varying Au coverage. As is shown in the figure, the equilibrium corrosion potential for SS316L with no Au is 0.05 V/NHE. For normal 20nm-Au/SS316L material with 100% Au coverage, the equilibrium potential is 0.465 V/NHE. For other intermediate cases, it is seen that the mixed potentials are more favored towards normal 20nm-Au/SS316L potential (i.e. 0.465 V/NHE). This is due to the fact that Au tends to passivate the bare SS316L substrate and moves the mixed potential more favorably towards close to 0.465 V/NHE. The anodic passivation protection is strongest at equilibrium corrosion potential (E_{corr}), and polarization from E_{corr} reduces the amount of protection (Fig. 11). The amount of protection for 75% Au coverage (normalized with surface area) is shown in Fig. 12. For typical fuel cell operating potentials of 0.8 V/NHE,

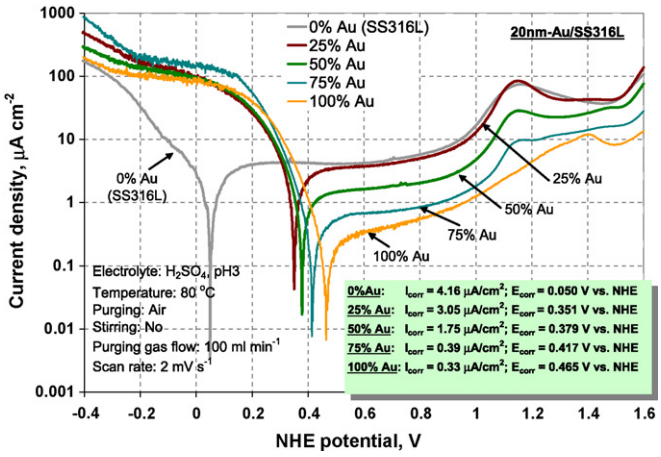

Fig. 10. Tafel plots for 20nm-Au/SS316L samples with varying Au coverage.

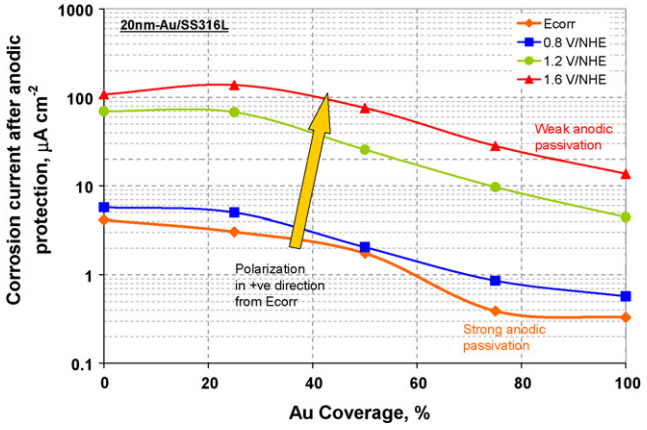

Fig. 11. Corrosion currents after anodic protection in samples with varying Au coverage.

a 70% protection can be realized for the uncovered SS316L substrate.

3.3. Mechanical properties

The mechanical properties (tensile strength, elongation, *n*-value) of 10nm-Au/SS316L are similar to those of SS316L base substrate (Table 2). This means that the Nanoclad process does not

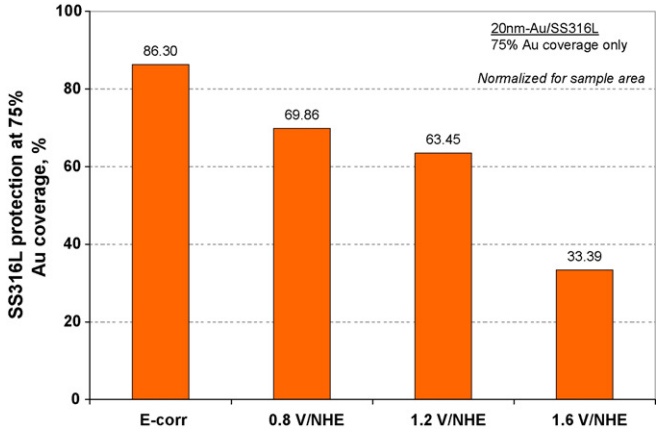

Fig. 12. Protection of SS316L base substrate with increasing polarization for 75% Au coverage.

Table 2
Mechanical properties[a] of 10nm-Au/SS316L material and bare SS316L material.

Property	Direction	10nm-Au/SS316L	Bare 316L
Tensile strength (MPa)	A[b]	594	600
	B[b]	577	583
Elongation (%)	A	50	53
	B	61	64
Strain hardening exponent (*n*-value)	A	0.43	0.41
	B	0.44	0.41

[a] Gauge is 0.1 mm in all cases.
[b] A is rolling direction and B is perpendicular to rolling direction.

change the properties of the base substrate. Since SS316L material has been the industry benchmark for formability of bipolar plate, no issues were foreseen in making stamped bipolar plates with 10nm-Au/SS316L.

4. Conclusions

Verification test methods developed to cover anticipated failure modes for bipolar plate materials were utilized to benchmark 10nm-Au/SS316L material. The area specific resistance for the 10nm-Au/SS316L flat sample is 0.9 $m\Omega\,cm^2$ while that for the formed bipolar plate is 6.3 $m\Omega\,cm^2$ at compaction force of 60 $N\,cm^{-2}$. The corrosion current densities were less than 1 $\mu A\,cm^{-2}$ at 0.8 V/NHE in 24 h potentiostatic experiment with air sparge simulating cathodic conditions. The material did not exhibit any active peaks under anodic conditions. Additionally, the material exhibited low current densities of less than 10 $\mu A\,cm^{-2}$ for high potentials under anodic (0.1 and 0.5 V/NHE) and cathodic (1.2 and 1.4 V/NHE) conditions, and up to 60 $\mu A\,cm^{-2}$ for cathodic (1.6 V/NHE) condition.

These results indicate that 10nm-Au/SS316L has excellent potential for its use in automotive fuel cells stacks. Additionally, due to use of a very thin Au coating, 10nm-Au/SS316L has the potential to meet the plate cost targets required for commercialization.

Acknowledgements

The authors would like to thank the team at Daido Steel (Japan) for providing the 10nm-Au/SS316L and 20nm-Au/SS316L samples, and for helpful discussions.

References

[1] H. Tawfik, Y. Hung, D. Mahajan, J. Power Sources 163 (2007) 755–767.
[2] H. Wang, M.A. Sweikart, J.A. Turner, J. Power Sources 115 (2003) 243–251.
[3] V. Mehta, J.S. Cooper, J. Power Sources 114 (2003) 32–53.
[4] A. Hermann, T. Chaudhuri, P. Spagnol, Int. J. Hydrogen Energy 30 (2005) 1297–1302.
[5] Atlas of Eh–pH diagrams, Geological Survey of Japan Open File Report No. 419, retrieved from web at http://www.gsj.jp/GDB/openfile/files/no0419/openfile419e.pdf on May 6, 2009.
[6] W. Yoon, X. Huang, P. Fazzino, K.L. Reifsnider, M.A. Akkaoui, J. Power Sources 179 (2008) 265–273.
[7] L.D. Burke, P.F. Nugent, Gold Bull. 30 (2) (1997).
[8] C.M. Vitus, A.J. Davenport, J. Electrochem. Soc. 141 (5) (1994).
[9] K. Juodkazis, et al., Electrochem. Commun. 1 (1999) 315–318.
[10] S. Takagi et al., U.S. Patent Application 20,060,159,971.